RSC Advances

PAPER

View Article Online
View Journal | View Issue

Cite this: *RSC Adv.*, 2022, **12**, 34571

Selective removal and recovery of Ni(II) using a sulfonic acid-based magnetic rattle-type ion-imprinted polymer: adsorption performance and mechanisms†

Weiye Zhang,[a] Xiujun Deng,[b] Siqing Ye,[a] Yan Xia,[a] Lingling Li,[a] Weili Li[a] and Hongxing He *[a]

It is significant to selectively remove Ni(II) ions from wastewater. A novel sulfonic acid-based magnetic rattle-type ion-imprinted polymer (Fe_3O_4@void@IIP-Ni(II)) was designed by taking advantage of the strong interaction between Ni(II) and sulfonic acid groups. Green polymerization was used to synthesize Fe_3O_4@void@IIP-Ni(II), which was then investigated using SEM, TEM, FT-IR, VSM, TGA, EDS, and XPS. The adsorption results indicated that the prepared imprinted material had a short adsorption equilibrium time (10 min), good magnetic responsiveness (about 5 seconds) and high adsorption capacity (44.64 mg g^{-1}) for Ni(II) at the optimal pH of 6.0. The removal rate of Ni(II) was up to 99.97%, and the adsorption process was spontaneous and endothermic, following the pseudo-secondary kinetic model and Langmuir model. The selectivity coefficients of the imprinted material were 4.67, 4.62, 8.94 and 9.69 for Ni(II)/Co(II), Ni(II)/Cu(II), Ni(II)/Pb(II) and Ni(II)/Zn(II), respectively. The regeneration and application of the imprinted material in actual water samples have been verified. Moreover, the mechanism of selective adsorption for Ni(II) was investigated by FTIR, XPS and density functional theory (DFT) calculation. The results showed that the imprinted sorbent has a strong binding ability with Ni(II), and the adsorption of Ni(II) on Fe_3O_4@void@IIP-Ni(II) was the result of the co-coordination of O atoms of the sulfonic acid groups and N atoms of –N–C=O groups in AMPS with Ni(II).

Received 1st November 2022
Accepted 24th November 2022

DOI: 10.1039/d2ra06918k

rsc.li/rsc-advances

1. Introduction

Heavy metals are important pollutants causing potential threats. The threat of heavy metal pollution is that they cannot be decomposed by microorganisms and tend to accumulate in living organisms.[1,2] Nickel is a typical heavy metal that mainly exists in the form of Ni(II) in electroplating, mining, battery, and other industrial wastewater. A small amount of nickel is beneficial to the human body, but high levels of Ni(II) can damage the central nervous system and lead to a variety of skin diseases and even cancers.[3,4] Different countries and organizations have strict regulations on the discharge limits of nickel-containing wastewater and the content of nickel in drinking water. For example, the maximum allowable discharge concentration of nickel-containing wastewater in China is 1.0 mg L^{-1}, and the permissible limit of nickel ions in drinking water recommended by the World Health Organization is 20 μg L^{-1}.[5,6] On the other hand, as a more expensive metal, the recovery of nickel is also very valuable, because it not only saves operating costs, but also reduces the total nickel usage, thus improving environmental safety. As a result, it is essential to develop a method that can efficiently and selectively separate and recover Ni(II) from wastewater.

So far, several methods used to remove Ni(II) include adsorption, chemical precipitation, membrane separation and ion exchange.[7–10] Among these methods, adsorption has been widely used because of its merits of facile operation, cost-effectiveness and high efficiency.[11] However, traditional adsorbents lack the selectivity separation for specific metal ions, which limits their application in specific metal recovery.

In recent years, ion imprinting polymers (IIPs) have attracted extensive attention due to their selective recognition of template ions. Compared to traditional imprinting techniques, surface imprinting has the advantages of fast adsorption kinetics, good selectivity and high adsorption capacity.[12,13] This technology requires various matrix materials to play a supporting role in the imprinting process. Currently, commonly used matrix materials include silica particles, graphene oxide (GO), chitosan (CTS), carbon nanotubes (CNTs) and Fe_3O_4 microspheres.[14–18]

[a]*Yunnan Key Laboratory of Food Safety Testing Technology, Kunming University, Kunming 650214, China. E-mail: hxhe0212@kmu.edu.cn*

[b]*School of Chemistry and Chemical Engineering, Yunnan Key Laboratory of Metal-Organic Molecular Materials and Device, Kunming University, Kunming 650214, China*

† Electronic supplementary information (ESI) available. See DOI: https://doi.org/10.1039/d2ra06918k

Due to the magnetic properties of Fe_3O_4 microspheres, its magnetic separation technology can well solve the problem of solid–liquid separation of imprinting materials in waste liquid, which has a great development prospect.[19] Recently, a rattle-type magnetic IIPs was constructed. Rattle-type structure is a core@void@shell structure. It can be described as a movable core encapsulated in a shell.[20] As an important extension of core–shell polymers, rattle-type polymers are mostly synthesized by a templating strategy in which the middle layer and the outer shell are prepared on a prefabricated core and the middle layer is subsequently removed. The large cavity volume between the inner core and the outer shell of the rattle-type polymers provides sufficient space for the loading of target ions.[21–23] The rattle-type magnetic imprinted polymer has not only magnetic sensitivity, high specific surface area, low density and higher adsorption capacity, but also has good selectivity for template ions.[24] Up to now, theoretical calculations based on density functional theory (DFT) have been used to design IIPs and reveal the adsorption mechanism.[25–27] According to previous work, sulfonic acid-based imprinted polymers have good adsorption selectivity for Ni(II).[28] Unfortunately, there are few reports on the affinity mechanism between Ni(II) and sulfonic acid groups by DFT calculations.

Herein, a novel sulfonic acid-based magnetic rattle-type Ni(II) ion-imprinted polymer was synthesized by green polymerization using water as porogen and AMPS as water-soluble functional monomer to selectively remove and recover Ni(II) from aqueous solution. The selective adsorption properties for Ni(II) were studied by batch adsorption experiments. It was characterized by FT-IR, SEM, TEM, EDS, VSM and TG, and the adsorption mechanism for Ni(II) was discussed by FT-IR, XPS and DFT calculations.

2. Experimental

2.1 Reagents

HCl and NaOH were purchased from Kolon Chemical Co. Ltd (Chengdu, China). $Ni(NO_3)_2\cdot 6H_2O$, $Co(NO_3)_2\cdot 7H_2O$, $Cu(NO_3)_2\cdot 2H_2O$, $Zn(NO_3)_2\cdot 7H_2O$ and $Pb(NO_3)_2$ were purchased from Beijing Chemical Plant (Beijing, China). 2-Acryloyl-2-methylpropionic acid (AMPS) was purchased from Aladdin Biochemical Technology Co. (Shanghai, China). Ammonium persulfate and sodium bisulfate were purchased from Windship Chemical Reagent Technology Co. (Tianjin, China). *N*,*N*′-Methylenebisacrylamide (MBA) was purchased from Maclean Biochemical Technology Co. (Shanghai, China). All aqueous solutions were prepared by deionized water.

2.2 Synthesis of magnetic Ni(II) ion-imprinted polymer (Fe_3O_4@SiO_2@IIP-Ni(II) and Fe_3O_4@void@IIP-Ni(II))

2.2.1 Preparation of Fe_3O_4 microspheres. Fe_3O_4 microspheres were synthesized by the solvothermal method. First, $FeCl_3\cdot 6H_2O$ (0.01 mol) was dissolved in 15 mL ethylene glycol with ultrasonic assistance. Sodium acetate (0.03 mol) was then dissolved in 15 mL of ethylene and 0.75 g of polyethylene glycol-2000 (PEG-2000) was added with the assistance of ultrasound until the mixture was homogeneous. Then the two solutions mentioned above were mixed and stirred for 30 min. After that, the mixture was sealed in a Teflon-lined stainless-steel autoclave and kept at 200 °C for 6 h. The hot solution was cooled to room temperature, and the black solid product was collected with a magnet and then washed with ethanol several times. The Fe_3O_4 magnetic nanospheres were obtained after drying in vacuum at 60 °C for 6 h.

2.2.2 Preparation of Fe_3O_4@SiO_2. 0.6 g Fe_3O_4 microspheres was ultrasonically dispersed in a mixed solution of 120 mL isopropanol and 90 mL deionized water for 15 min, and then 11 mL ammonia (28%, w/w) and 2 mL TEOS were added to the suspension and mechanically stirred at room temperature for 12 h. Finally, the product was washed successively with deionized water and ethanol to neutral and dried under vacuum at 40 °C for 24 h to obtain Fe_3O_4@SiO_2.

2.2.3 Preparation of Fe_3O_4@SiO_2@VTMOS. 0.2 g Fe_3O_4 was sonicated and dispersed in 150 mL absolute ethanol, then mechanically stirred, during which 1 mL VTMOS was slowly added. The mixture was mechanically stirred at 30 °C for 8 h. After washing with methanol for three times, the products were cultured with 1 mol L^{-1} HCl for 12 h. Finally, vinyl-modified Fe_3O_4@SiO_2 was obtained by vacuum drying at 40 °C for 24 h.

2.2.4 Synthesis of Fe_3O_4@SiO_2@IIP-Ni(II) and Fe_3O_4@SiO_2@NIP-Ni(II). 2 mmol $Ni(NO_3)_2\cdot 6H_2O$ and 4 mmol AMPS were added to 50 mL deionized water and stirred magnetically at room temperature. After stirring for 0.5 h, 0.15 g Fe_3O_4@SiO_2@VTMOS was added and stirred for 12 h. Then 6 mmol MBA, 0.1 g ammonium persulfate and 0.05 g sodium bisulfite were added and bubbled with high purity argon for 30 min to eliminate oxygen and then sealed. After that, the mixture was heated in a water bath at 50 °C and magnetically stirred for 5 h. Finally, the obtained polymers were separated by a magnet, washed with methanol, hydrochloric acid and deionized water to neutral and dried in vacuum at 40 °C for 12 h to obtain Fe_3O_4@SiO_2@IIP-Ni(II).

The synthesis of Fe_3O_4@SiO_2@NIP-Ni(II) adsorbent was roughly the same as the above steps, except that $Ni(NO_3)_26H_2O$ was not introduced and HCl was not used for washing.

2.2.5 Synthesis of Fe_3O_4@void@IIP-Ni(II) and Fe_3O_4@void@NIP-Ni(II). Fe_3O_4@SiO_2@IIP-Ni(II) spheres were dispersed into 50 mL of HF aqueous solution (0.5%, w/w) and reacted for 20 min. The obtained Fe_3O_4@void@IIP-Ni(II) spheres were washed with deionized water to neutral and dried in a drying oven at 50 °C for 24 h. The synthesis process of Fe_3O_4@void@IIP-Ni(II) is shown in Fig. 1.

Fe_3O_4@void@NIP-Ni(II) spheres were prepared using the same procedure.

2.3 Batch adsorption experiments

Batch adsorption experiments were performed by adding a certain amount of sorbent to a certain volume of metal ion solution, and the mixture was shaken for a certain time at 25 °C. The concentrations of all metal ions were determined by ICP-OES. Each adsorption experiment was conducted in triplicate.

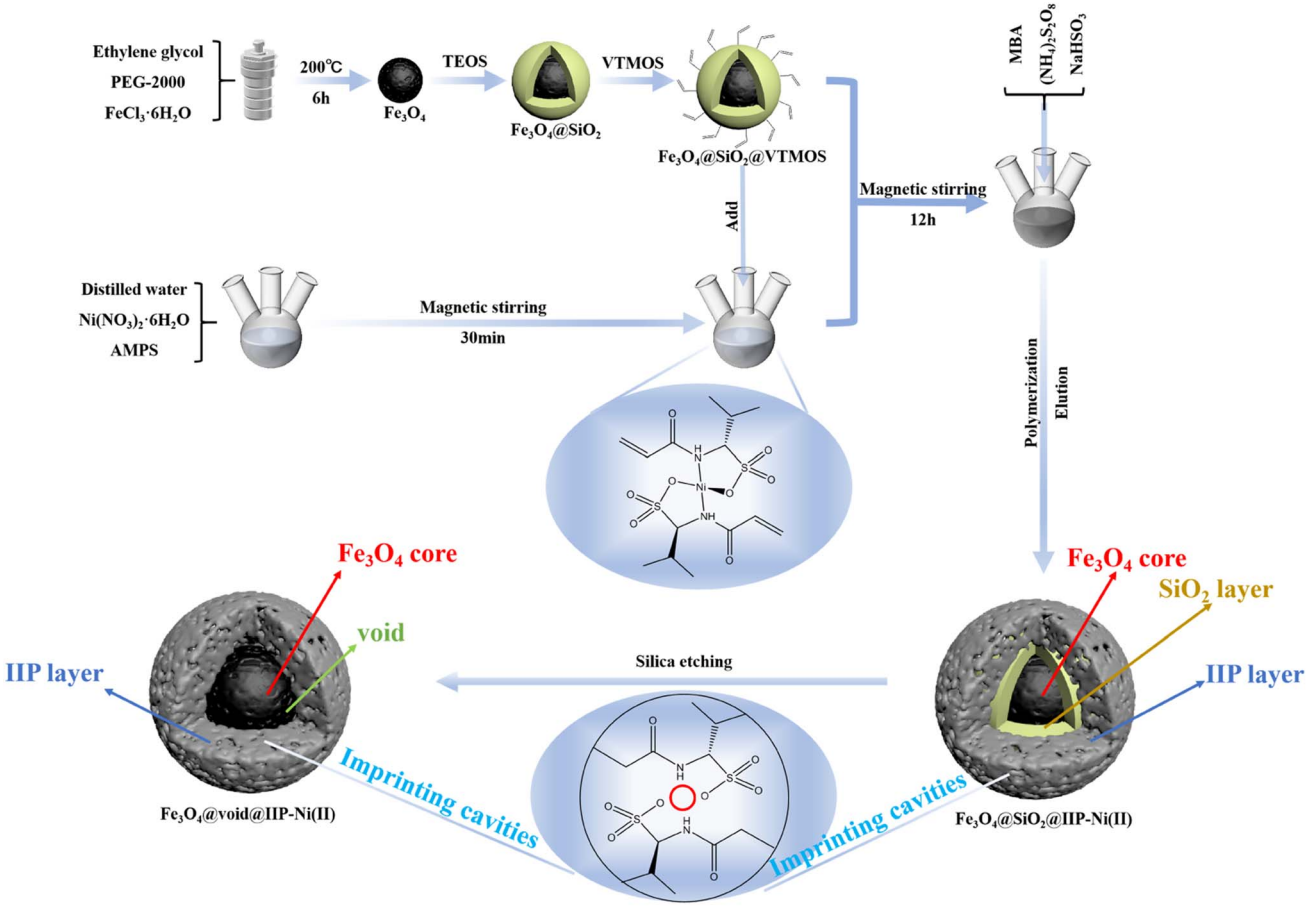

Fig. 1 Scheme for preparation of Fe_3O_4@void@IIP-Ni(II).

The adsorption capacity was calculated according to the following eqn (1).[29]

$$q = \frac{c_i - c_f}{1000W} \times V \quad (1)$$

where q (mg g^{-1}) is the adsorption capacity, c_i (mg L^{-1}) and c_f (mg L^{-1}) are the initial and final concentrations of metal ions, respectively; V (mL) is the volume of the solution; W (g) is the amount of sorbent.

The effect of pH on Ni(II) adsorption was examined by adding 20 mg sorbent into 20 mL 100 mg L^{-1} Ni(II) ion solution with varying pH values at 25 °C for 2 h. The pH of the solution was adjusted by HCl and NaOH solution. The effect of contact time on Ni(II) adsorption was determined by adding 50 mg sorbent into 50 mL 100 mg L^{-1} Ni(II) ion solution at different contact times at 25 °C and pH 6.0 for 60 min. Samples were taken out from the solution at various time intervals until saturated adsorption was reached. To evaluate the effect of initial concentrations on Ni(II) adsorption, 20 mg sorbent was added to 20 mL Ni(II) ion solution with varying concentrations (25–200 mg L^{-1}) at 25 °C and pH 6.0 for 2 h.

In the selective adsorption experiment, 20 mg adsorbent was added to 20 mL mixed solution containing 5 mg L^{-1} Ni^{2+}, Co^{2+}, Cu^{2+}, $Zn^{2+}$and Pb^{2+}, and vibrated at 25 °C for 2 h. Finally, the ion concentration in the filtrate was detected by ICP-OES. The distribution ratio (D), the selectivity coefficient (k) and the relative selectivity coefficient (k') were calculated according to the following eqn (2)–(4).[15]

$$D = \frac{(C_0 - C_e)}{C_e} \times \frac{V}{W} \quad (2)$$

$$k = \frac{D_{Ni}}{D_M} \quad (3)$$

$$k' = \frac{k_{IIP}}{k_{NIP}} \quad (4)$$

where C_0 (mg L^{-1}) and C_e (mg L^{-1}) are the initial and equilibrium concentrations of metal ions, V (mL) is the volume of metal ion solution, W (g) is the mass of sorbent, M represents other competitive metal ions.

2.4 Theoretical calculation

Density functional theory calculations were performed utilizing the Gaussian 16 W, the geometry optimization of the functional group and metal ion complexes were performed at PBE1PBE (solvent = water, D3 BJ)/def2svp level, and def2tzvp basis set was used to calculate the adsorption energy (E_{ad}).[27] The adsorption energy (E_{ad}) between AMPS and the different metal ions was calculated by eqn (5).

$$E_{ad} = E_{(total)} - E_{(AMPS)} - E_{(adsorbates)} \quad (5)$$

where $E_{(total)}$, $E_{(AMPS)}$ and $E_{(adsorbates)}$ are the total energy of the adsorption complex, the adsorbent AMPS and the adsorbates, respectively.

3. Results and discussion

3.1. Characterization of absorbents

3.1.1 Morphology study. Fig. 2 shows the SEM images of Fe_3O_4, Fe_3O_4@SiO_2, Fe_3O_4@SiO_2@VTMOS, Fe_3O_4@SiO_2@IIP-Ni(II) and Fe_3O_4@void@IIP-Ni(II). It can be seen that all materials were roughly in the shape of the ball. The surface of Fe_3O_4 prepared by the solvothermal method was rough (Fig. 2(a)), and the particle size was about 150 nm. After grafting silica gel on the surface of Fe_3O_4 (Fig. 2(b)), the Fe_3O_4@SiO_2 surface became smoother and its particle size was larger than that of Fe_3O_4, the particle size was about 200 nm, which can be inferred that silica gel has been coated on the surface of Fe_3O_4. As shown in Fig. 2(c), compared with Fe_3O_4@SiO_2, the particle size of Fe_3O_4@SiO_2@VTMOS was further increased to about 400 nm, this indicated that vinyl was grafted onto the surface of Fe_3O_4@SiO_2. By introducing the imprinted polymer layer on the surface of Fe_3O_4@SiO_2@VTMOS (Fig. 2(d)), it can be clearly seen that the spherical Fe_3O_4@SiO_2@IIP-Ni(II) gathered together and became rough again. As shown in Fig. 2(e), the surface morphology of the Fe_3O_4@void@IIP-Ni(II) sphere was similar to broccoli, and the interior of the microsphere obtained by HF solution treatment had many mass transfer channels for rapid entry of template ions, which improved the adsorption rate of the microspheres. All these results showed that the magnetic rattle-type Fe_3O_4@void@IIP-Ni(II) microsphere was successfully prepared after five preparation steps.

Fig. 3 shows the TEM images of Fe_3O_4@SiO_2, Fe_3O_4@SiO_2@IIP-Ni(II) and Fe_3O_4@void@IIP-Ni(II). The dark Fe_3O_4 core can be clearly seen in each image. As shown in Fig. 3(a), the light-colored thin layer outside the Fe_3O_4 core is coated with silica gel. In Fig. 3(b), a thin layer appears outside the silica gel layer, which is the imprinted thin layer grafted onto the surface of Fe_3O_4@SiO_2. Fig. 3(c) shows the Fe_3O_4@SiO_2@IIP-Ni(II) treated with HF solution. Compared with Fig. 3(b), it can be seen that there is only one continuous thin layer outside the Fe_3O_4 core, and a hollow structure is formed between the thin layer and the core. It is the result of HF acid etching of the silica layer while retaining only the imprinted layer.

In addition, EDS spectra of Fe_3O_4@void@IIP-Ni(II) before and after Ni(II) ion adsorption are shown in Fig. S1.† Before and after Ni(II) adsorption, the content of S was relatively high, 6.78% (wt%) and 6.09% (wt%), respectively, while the content of Si is relatively low, 0.06% (wt%) and 0.26% (wt%), respectively. The high content of the former is mainly due to the introduction of S in the sulfonic acid group on the functional monomer AMPS. It can also proved that AMPS was successfully introduced into the adsorbent. The low content of the latter is mainly due to the etching of SiO_2 by HF solution, which further confirms the generation of hollow structures. The obvious signal of Ni changed considerably before and after adsorption, with the Ni content changing from 0 (wt%) to 4.47 (wt%). The former indicated that Ni(II) elution was complete after the imprinting process, while the latter confirmed the existence of the adsorption properties of Fe_3O_4@void@IIP-Ni(II).

3.1.2 FT-IR. Fig. 4A shows the infrared spectrum of Fe_3O_4 (a), Fe_3O_4@SiO_2 (b), Fe_3O_4@SiO_2@VTMOS (c), Fe_3O_4@SiO_2@-IIP-Ni(II) (d), Fe_3O_4@void@IIP-Ni(II) (e) and Fe_3O_4@void@IIP-Ni(II) after adsorption (f), respectively. In the infrared spectrum of Fe_3O_4 (Fig. 4A(a)), the characteristic peak of 585 cm^{-1} was attributed to the stretching vibration of Fe–O.[30] Moreover, this characteristic peak was present in the IR spectra of all samples, it proved that Fe_3O_4 core was present in all materials. After TEOS-treated Fe_3O_4, two peaks appeared at 1630 cm^{-1} and 1083 cm^{-1}. The former was due to the existence of O–H and the latter was the stretching vibration of Si–O, which confirmed that Fe_3O_4 was wrapped by SiO_2 (Fig. 4A(b)).[24] The peak at 1629 cm^{-1}

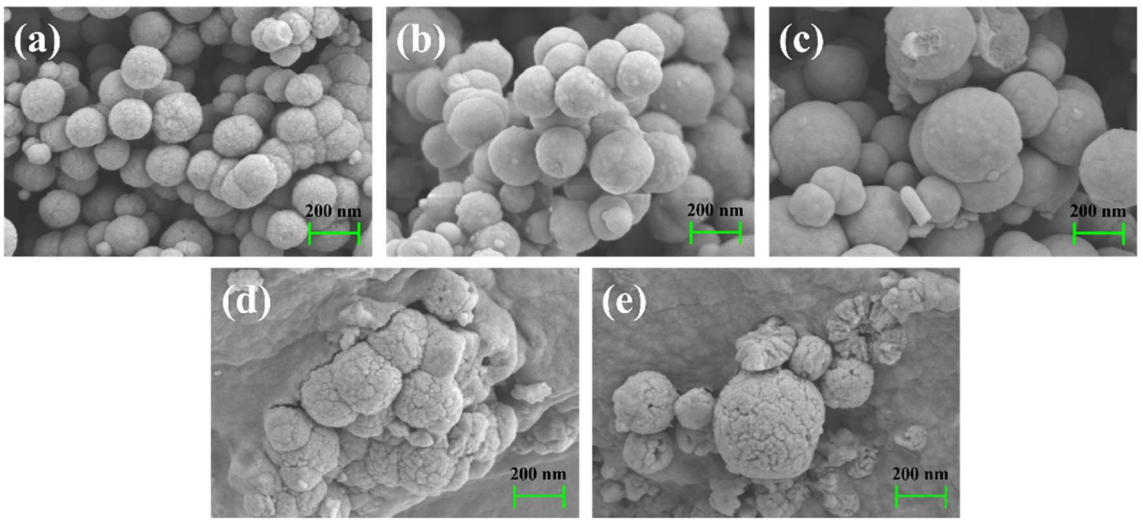

Fig. 2 SEM images of (a) Fe_3O_4 (b) Fe_3O_4@SiO_2 (c) Fe_3O_4@SiO_2@VTMOS (d) Fe_3O_4@SiO_2@IIP-Ni(II) and (e) Fe_3O_4@void@IIP-Ni(II).

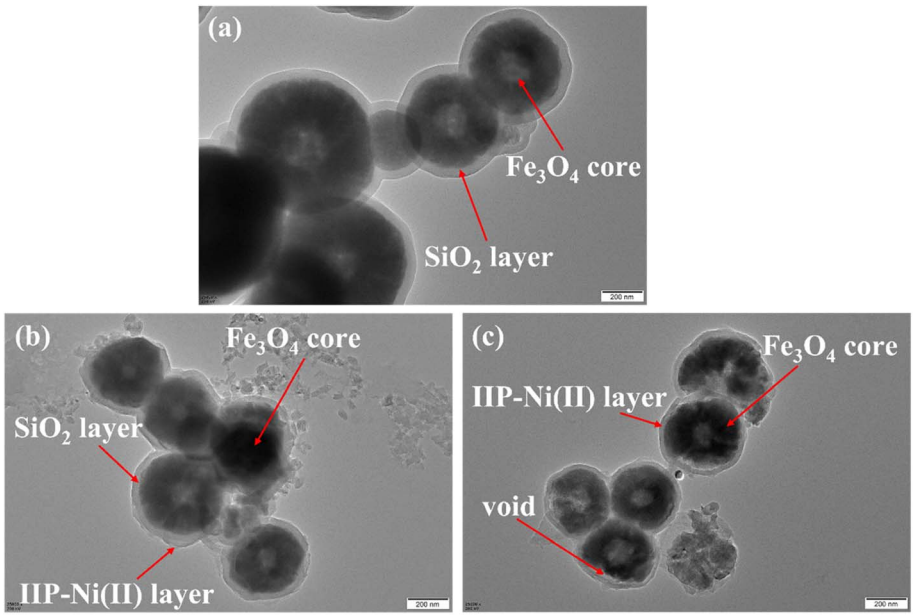

Fig. 3 TEM images of (a) Fe_3O_4@SiO_2, (b) Fe_3O_4@SiO_2@IIP-Ni(II) and (c) Fe_3O_4@void@IIP-Ni(II).

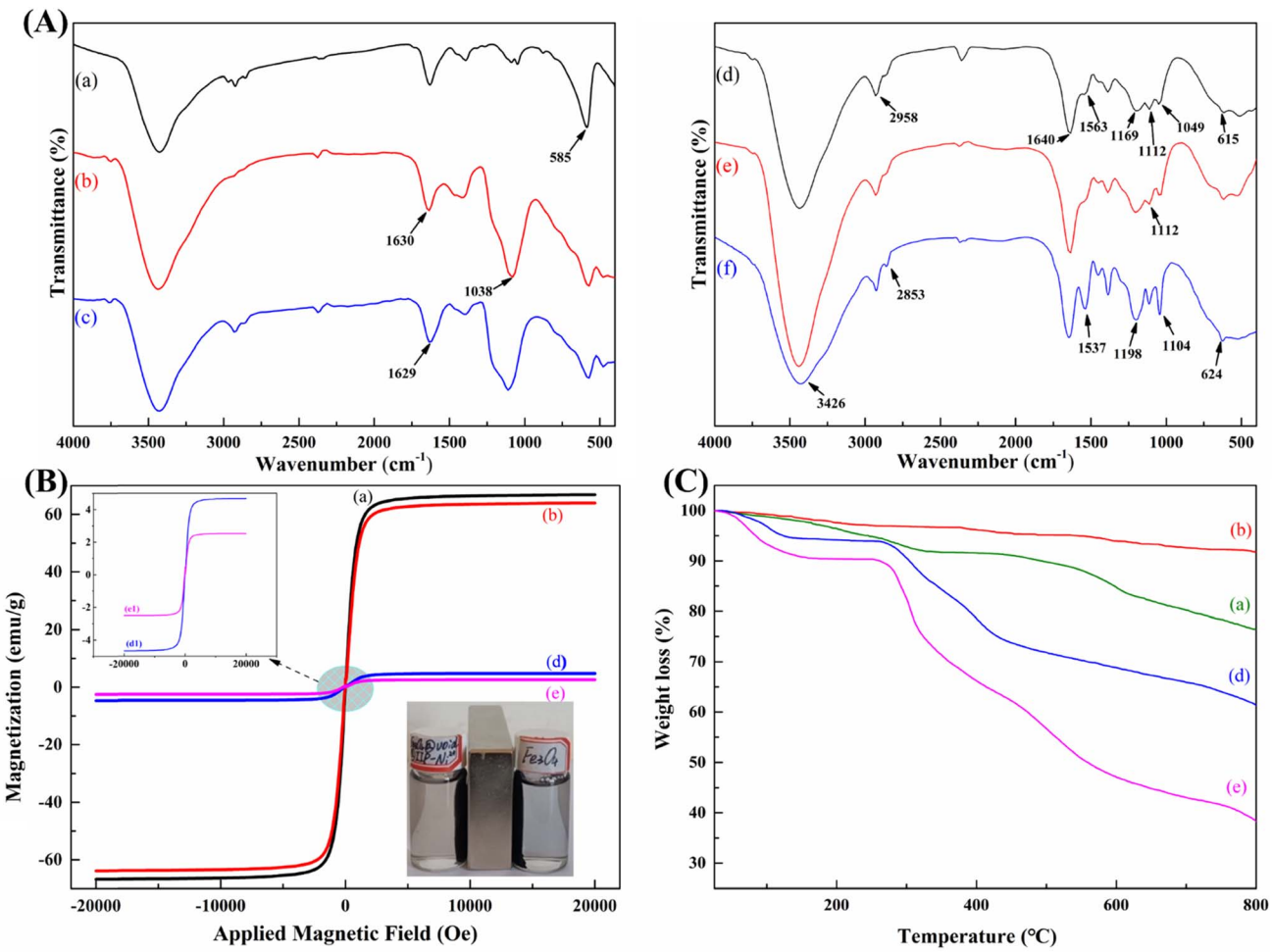

Fig. 4 FT-IR spectra (A), magnetic hysteresis loops (B) and TG curves (C) of (a) Fe_3O_4, (b) Fe_3O_4@SiO_2, (c) Fe_3O_4@SiO_2@VTMOS, (d) Fe_3O_4@SiO_2@IIP-Ni(II), (e) Fe_3O_4@void@IIP-Ni(II) and (f) Fe_3O_4@void@IIP-Ni(II) after adsorption.

was caused by C=C stretching vibration. This proved that the double bond was successfully grafted onto the surface of Fe_3O_4@SiO_2 (Fig. 4A(c)).[31] As shown in Fig. 4A(d), 2958 cm^{-1} was the stretching vibration of C–H, 1640 cm^{-1} was the stretching vibration of C=O, 1169 cm^{-1}, 1049 cm^{-1} and 615 cm^{-1} were the stretching vibration of S=O and the asymmetric stretching vibration of S–O, respectively,[32] 1563 cm^{-1} was the characteristic peak of N–H.[33] The appearance of these peaks indicated that the polymer AMPS-*co*-MBA was successfully grafted onto the Fe_3O_4@SiO_2@VTMOS surface. In the IR spectrum of Fe_3O_4@void@IIP-Ni(II) shown in Fig. 4A(e), compared with Fig. 4A(d), the intensity of the Si–O peak at 1112 cm^{-1} was weakened, which proved the shedding of the silicon shell and the formation of the rattle-type structure.

3.1.3 Magnetic response performance. Hysteresis loop refers to the phenomenon of magnetic hysteresis caused by ferromagnetic materials when the magnetic field strength changes periodically, forming a closed magnetization curve. Fig. 4B presents the magnetic hysteresis loops of Fe_3O_4 (Fig. 4B(a)), Fe_3O_4@SiO_2 (Fig. 4B(b)), Fe_3O_4@SiO_2@IIP-Ni(II) (Fig. 4B(d)) and Fe_3O_4@void@IIP-Ni(II) (Fig. 4B(e)). As shown in Fig. 4B, the saturation magnetization of Fe_3O_4 at room temperature is 66.79 emu g^{-1}, while that of Fe_3O_4@SiO_2 decreases to 63.89 emu g^{-1}. Although the silicon coating has a partial effect on the magnetism, the effect is minimal and the overall magnetism remains strong. After grafting the imprinted thin layer, the magnetic saturation intensity decreased significantly to 4.67 emu g^{-1} for Fe_3O_4@SiO_2@IIP-Ni(II) and 2.51 emu g^{-1} for Fe_3O_4@void@IIP-Ni(II), which may be due to the destruction of the Fe_3O_4 core by HF acid etching and the formation of hollow structure during the grafting of the imprinted thin layer. Remarkably, it is sufficient to achieve a quick solid–liquid separation under external magnetic field conditions. Here is a video of the use of a magnet to separate the imprinted microspheres from aqueous solution (see the ESI†). As seen in the video, the Fe_3O_4@void@IIP-Ni(II) nanospheres (left) can easily complete the magnetic separation process from the aqueous solution in about 5 seconds. This indicated that Fe_3O_4@void@IIP-Ni(II) microparticles had good magnetic responsiveness.

3.1.4 Thermal stability. TGA was used to analyze the thermal stability of the novel magnetic Ni(II) ion imprinting materials. The thermal stability was investigated in the range of 25 °C to 800 °C at a heating rate of 10 °C min^{-1} under a nitrogen atmosphere. The weight loss of Fe_3O_4 (Fig. 4C(a)) and Fe_3O_4@SiO_2 (Fig. 4C(b)) is 8.22% and 23.5%, respectively, from 25 °C to 800 °C. This is because SiO_2 was successfully coated on the surface of Fe_3O_4. Based on the SiO_2 modification, the thermal stability of Fe_3O_4@SiO_2 is improved. For Fe_3O_4@SiO_2@IIP-Ni(II) (Fig. 4C(d)) and Fe_3O_4@void@IIP-Ni(II) (Fig. 4C(e)), when the temperature is increased from room temperature to about 150 °C, their weight loss are 5.56% and 9.21%, respectively, which is mainly due to the loss of physically adsorbed water. When the temperature increases from 150 °C to 260 °C, the weight loss rates of both are very small, only 0.54% and 0.73%, which may be due to the thermal stability of the imprinted polymer thin layer (AMPS-*co*-MBA) on the material surface. However, the weight loss rate of both increases significantly at temperature above 260 °C, which may be due to the decomposition of the imprinted polymer layer on the material surface. In general, Fe_3O_4@void@IIP-Ni(II) has higher weight loss than Fe_3O_4@SiO_2@IIP-Ni(II) because the former has a higher percentage of organic decomposable substances. It was confirmed that the magnetic Ni(II) ion imprinted material synthesized through several steps has good thermal stability at temperatures below 260 °C.

3.2 Adsorption performance

3.2.1 Effect of reagent dosage on adsorption performance. The amount and ratio of each component have a crucial influence on their adsorption properties during the polymerization of imprinted polymers.[34] Therefore, we tried the effects of different ratios of template ions, functional monomers and crosslinkers on the adsorption properties of ion imprinted polymers, the results are shown in Fig. S2.† When the dosage ratio of template ion, functional monomer and crosslinker was 1 : 2 : 4, the amount of template ion and functional monomer was less, and the number of imprinting sites was less, resulting in smaller adsorption capacity.[35] The adsorption capacity increased at the dosage ratio of 2 : 4 : 4, and reached a maximum at the dosage ratio is 2 : 4 : 6. Whereas, the adsorption capacity gradually decreased as the dosage of crosslinking agent increased from 6 mmol to 10 mmol. This is because the increase of crosslinkers makes the surface of the imprinted polymer dense, resulting in the encapsulation of the imprinted sites and the difficulty of elution of template ions.[36] Overall, optimal amounts of template (Ni(II)), monomer (AMPS) and crosslinker (MBA) were 2 mmol, 4 mmol and 6 mmol, respectively.

3.2.2 Effect of pH on the adsorption. Considering that nickel ion will hydrolyze when pH > 8.0,[37] the effect of different pH on the adsorption properties of Ni(II) was studied at room temperature when the concentration of Ni(II) was 50 mg L^{-1} and pH was 2.0–8.0. As shown in Fig. S3,† when the pH value of the solution is 6.0, Fe_3O_4@void@IIP-Ni(II) and Fe_3O_4@SiO_2@IIP-Ni(II) reach the maximum adsorption capacity of 28.77 mg g^{-1} and 36.48 mg g^{-1}, respectively. When pH < 3.0, the protonation of the active site reduces the adsorption capacity. And when pH > 6.0, partial hydrolysis of Ni(II) forms $Ni(OH)_2$, resulting in a decrease of the free Ni(II) concentration in the solution and thus a decrease in the adsorption capacity. In our case, the adsorption capacity of the two adsorbents was relatively optimal when the solution pH = 6.0.

3.2.3 Adsorption kinetics. In order to study adsorption kinetics, the adsorption equilibrium time of Ni(II) on adsorbents was investigated at 25 °C, pH = 6.0 and an initial Ni(II) concentration of 50 mg L^{-1}. It can be seen from Fig. 5a that the adsorption capacity of the four adsorbents increased rapidly in the first 10 min. This is because there are many imprinted sites on the surface of the imprinted polymer at the initial stage of adsorption. After 10 minutes, the adsorption rate increased slowly as the surface imprinted sites were gradually occupied, so it was considered that the adsorption equilibrium could be

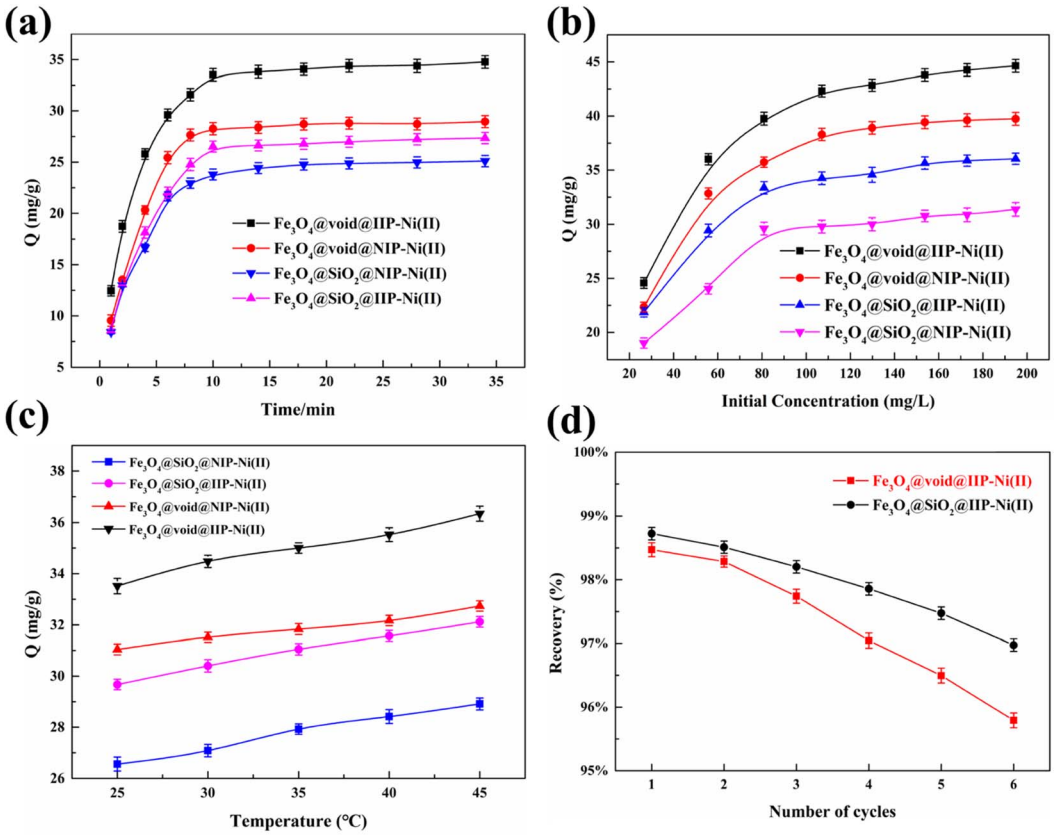

Fig. 5 Effect of time (a), Ni(II) initial concentration (b), temperature and (c) desorption and reusability (d) on the adsorption.

reached around 10 min. The adsorption capacity of IIP was higher than that of NIP with or without silica gel removal, mainly because more cavities formed by the elution of template ions.

To further investigate the adsorption kinetic mechanism of imprinted materials, pseudo-first-order kinetics and pseudo-second-order kinetics models were used for the linear fitting of data. The linear form of the pseudo-first-order kinetics and the pseudo-second-order kinetics models are expressed as follows eqn (6) and (7).[12]

$$\ln(q_e - q_t) = \ln q_e - k_1 t \quad (6)$$

$$\frac{t}{q_t} = \frac{1}{k_2 q_e^2} + \frac{1}{q_e} t \quad (7)$$

where q_t (mg g^{-1}) and q_e (mg g^{-1}) are the adsorption capacities of Ni(II) ion at time t and at equilibrium, respectively. k_1 (min^{-1}) is the rate constant of the first-order model, k_2 (g min^{-1} mg^{-1}) is the rate constant for pseudo-second-order model at the equilibrium.

Fig. S4† present the plots of pseudo-first-order and pseudo-second-order kinetic models of the four adsorbents. The kinetic parameters of the two models are shown in Table 1. The results showed that the correlation coefficients fitted by the pseudo-second-order kinetic model (R_2^2) were better than those of the pseudo-first-order kinetic model (R_1^2), and they are 0.9977, 0.9983, 0.9989 and 0.9982, respectively. Besides, the q_e value fitted by pseudo-second-order kinetic was closer to the experimental value. It can be concluded that the adsorption of Ni(II) ion onto Fe_3O_4@void@IIP-Ni(II), Fe_3O_4@void@NIP-Ni(II), Fe_3O_4@SiO_2@IIP-Ni(II) and Fe_3O_4@SiO_2@NIP-Ni(II) was a chemical adsorption process.

3.2.4 Adsorption isotherms. The equilibrium adsorption isotherm is significant in describing the adsorption interaction between the adsorbates and adsorbents. The adsorption isotherm study was conducted at 25 °C and pH = 6.0 with the initial concentration of Ni(II) in the range of 25–200 mg L^{-1}. Fig. 5b shows the effect of the initial concentration of Ni(II) on the adsorption. It can be seen that the adsorption capacity increased with the increase of the initial concentration, but when the initial concentration was higher than 100 mg L^{-1}, the adsorption capacity increased very slowly until the adsorption equilibrium was reached. The maximum adsorption capacities of Fe_3O_4@void@IIP-Ni(II), Fe_3O_4@void@NIP-Ni(II), Fe_3O_4@SiO_2@IIP-Ni(II) and Fe_3O_4@SiO_2@NIP-Ni(II), were 44.64 mg g^{-1}, 39.75 mg g^{-1}, 36.05 mg g^{-1} and 31.37 mg g^{-1}, respectively. Moreover, the IIPs sorbents had larger adsorption capacity than that of NIPs sorbents. For instance, the maximum adsorption capacity of Fe_3O_4@void@IIP-Ni(II) was much higher than that of Fe_3O_4@void@NIP-Ni(II), and the maximum adsorption capacity of Fe_3O_4@SiO_2@IIP-Ni(II) was much higher than that of Fe_3O_4@SiO_2@NIP-Ni(II), indicating that imprinting technology enhances the adsorption capacity of the adsorbent. It is

Table 1 Parameters for the pseudo-first-order and pseudo-second-order kinetic models

		Pseudo-first-order kinetic models			Pseudo-second-order kinetic models		
Adsorption kinetic model	$q_{e,exp}$	k_1	$q_{e,cal}$	R_1^2	k_2	$q_{e,cal}$	R_2^2
Fe_3O_4@void@IIP-Ni(II)	27.35	0.1428	11.81	0.8905	0.01741	29.33	0.9977
Fe_3O_4@void@NIP-Ni(II)	25.10	0.1323	9.884	0.8850	0.02152	26.71	0.9983
Fe_3O_4@SiO_2@IIP-Ni(II)	34.77	0.1275	12.55	0.8714	0.01821	36.58	0.9989
Fe_3O_4@SiO_2@NIP-Ni(II)	28.96	0.1679	10.64	0.8640	0.01991	30.77	0.9982

probably because of the introduction of template ions, more imprinted sites were generated, resulting in a larger adsorption capacity of IIPs than NIPs. Notably, the maximum adsorption capacity of Fe_3O_4@void@IIP-Ni(II) (or Fe_3O_4@void@NIP-Ni(II)) had much higher than that of Fe_3O_4@SiO_2@IIP-Ni(II) (or Fe_3O_4@SiO_2@NIP-Ni(II)), indicating the imprinted polymers with rattle-type structure by etching silica layer helps to improve the adsorption capacity. Furthermore, the adsorption properties of Fe_3O_4@void@IIP-Ni(II) were compared with those previous reported sorbents (listed in Table S1†), and the prepared Fe_3O_4@void@IIP-Ni(II) displays a faster adsorption rate, larger adsorption capacity and higher removal efficiency.

To better study the adsorption mechanism of adsorbent, the data were fitted by Langmuir and Freundlich isotherm models. The linear expressions of the two models were as follows eqn (8) and (9).[12]

Langmuir isotherm:

$$\frac{c_e}{q_e} = \frac{K}{q_m} + \frac{c_e}{q_m} \quad (8)$$

Freundlich isotherm:

$$\ln q_e = \frac{1}{n}\ln C_e + \ln K_F \quad (9)$$

where q_e (mg g^{-1}) is the adsorption capacity of Ni(II) ion at equilibrium, c_e (mg L^{-1}) is the equilibrium concentration of Ni(II) ion in the solution, q_m (mg g^{-1}) is the maximal adsorption capacity of Ni(II) ion, K (L g^{-1}) is a constant in the Langmuir model. K_F and n are the constants in the Freundlich model.

The plots of adsorption isotherm models are presented in Fig. S5,† and the parameters of two models are given in Table 2. It can be seen that Langmuir model can better describe the adsorption mechanism of Ni(II) on imprinted materials. The correlation coefficients of Fe_3O_4@void@IIP-Ni(II), Fe_3O_4@void@NIP-Ni(II), Fe_3O_4@SiO_2@IIP-Ni(II) and Fe_3O_4@SiO_2@NIP-Ni(II) were 0.9982, 0.9973, 0.9988 and 0.9965, respectively. In addition, the maximum adsorption capacity fitted by Langmuir model was closer to the experimental value. As a result, Langmuir model may be utilized to describe the adsorption process, indicating that Ni(II) ion adsorption on the adsorbents was a monolayer adsorption on the adsorbent surface.

3.2.5 Thermodynamic study. The effect of temperature on the adsorption performance of the materials was discussed at a solution pH = 6.0, an initial Ni(II) concentration of 50 mg L^{-1} and a temperature range of 25–45 °C. Fig. 5c shows the influence curve of temperature on its adsorption capacity. The results showed that the increase of temperature was beneficial to the adsorption of Ni(II). On the one hand, this may be because higher temperature changes the pore size of the adsorbent, allowing more Ni(II) ions to diffuse into the adsorbent. On the other hand, the higher temperature enhances the chemical affinity of Ni(II) ions to the adsorbent surface, resulting in more chemical interactions during the adsorption process.

The relevant thermodynamic parameters were calculated to clarify the thermodynamic mechanism of the adsorption process. The Gibbs free energy (ΔG), enthalpy (ΔH) and entropy (ΔS) were evaluated as follows eqn (10) and (11).[4]

$$\Delta G = -RT\ln(1000K_c) \quad (10)$$

$$\ln K_c = -\frac{\Delta H}{RT} + \frac{\Delta S}{R} \quad (11)$$

where R is the universal gas constant (8.314 J mol^{-1} K^{-1}), T is absolute temperature (K), K_c is ($K_c = q_e/c_e$) equilibrium constant. The value of ΔG was calculated directly from the above relations, the slope and the intercept of the $\ln K_c$ *versus* $1/T$ were utilized to obtain the values of ΔH and ΔS as shown in Fig. S6,† the calculated values of thermodynamic parameters are reported in Table S2.†

The negative values of ΔG suggested the feasibility and spontaneity for Ni(II) adsorption, the positive values of ΔH

Table 2 Parameters for the Langmuir and Freundlich adsorption isotherm models

		Langmuir adsorption isotherm			Freundlich adsorption isotherm		
Adsorption isothermal model	$q_{e,exp}$	K_L	q_m	R_L^2	K_F	n	R_F^2
Fe_3O_4@void@IIP-Ni(II)	44.64	23.97	50.85	0.9982	10.61	3.513	0.8830
Fe_3O_4@void@NIP-Ni(II)	39.75	22.01	44.90	0.9973	9.977	3.627	0.8657
Fe_3O_4@SiO_2@IIP-Ni(II)	36.05	19.42	39.95	0.9988	10.64	4.137	0.8892
Fe_3O_4@SiO_2@NIP-Ni(II)	31.37	20.58	34.84	0.9965	8.893	4.020	0.8837

revealed that the adsorption process was endothermic and the higher temperature could accelerate reaction kinetics to promote adsorption. Notably, the obtained ΔH value was between 28 and 46, which can be inferred that the adsorption of Ni(II) on adsorbents was mainly driven by coordination interaction, supplemented by electrostatic interaction.[38] As for ΔS, the positive value indicated an increase in the randomness of adsorption process, which may be due to the release of water molecules on the adsorbent during Ni(II) adsorption.

3.3 Selectivity and reusability

To investigate the adsorption selectivity of four adsorbents for trace Ni(II), the mixed solutions of Ni(II), Co(II), Cu(II), Zn(II) and Pb(II) with initial concentration of 5 mg L^{-1} were selected. The results showed that Fe_3O_4@void@IIP-Ni(II) exhibited an excellent adsorption performance for Ni(II) than Co(II), Cu(II), Zn(II) and Pb(II) ions, and the removal rate of for Ni(II) was as high as 99.97%, close to 100% (shown in Fig. 6). Meanwhile, Fe_3O_4@void@IIP-Ni(II) showed higher removal efficiency for all metal ions than that of Fe_3O_4@SiO_2@IIP-Ni(II), which was mainly due to the formation of the rattle-type structure by silicon corrosion, thus greatly enhancing the adsorption capacity. Remarkably, whether the silicon layer was etched or not, both IIPs and NIPs showed the highest removal efficiency for Ni(II), while the removal efficiency for Zn(II) was not high. To explore those experimental results, the binding energies of different metal ions to AMPS were calculated using the DFT method, and the calculated results are shown in Fig. 7. It can be seen that the calculated results are in high agreement with the experimental results, and the binding energies of AMPS with these metal ions are Ni(II), Co(II), Cu(II), Pb(II) and Zn(II) from high to low. This means that AMPS has good affinity with Ni(II) in aqueous solution, and the selected monomer AMPS is suitable for the adsorption of Ni(II).

From the perspective of k values as listed in Table S3,† the values of NIPs with or without silicon etching were consistent with the calculation results by DFT method; however, the k values of IIPs were partially inconsistent with those of DFT, for example, $k_{Ni(II)/Co(II)}$ was slightly larger than $k_{Ni(II)/Cu(II)}$ for Fe_3O_4@void@IIP-Ni(II), which was mainly due to the imprinting effect. Notably, the k values of Ni(II)/Co(II), Ni(II)/Cu(II), Ni(II)/Pb(II), and Ni(II)/Zn(II) for Fe_3O_4@void@IIP-Ni(II) were 4.67, 4.62, 8.94, and 9.69, respectively, which were all greater than 1, indicating that the imprinted adsorbent had a high selectivity for Ni(II).

The reusability of the sorbent is one of the most critical parameters for its practical application. The reuse properties of two imprinted adsorbents was explored by six adsorption–desorption experiments using 2 mol L^{-1} HCl solution as the eluent. The results are shown in Fig. 5d. It can be seen that after six cycles, the recovery of Ni by both imprinted adsorbents was still above 95%. The results showed that two magnetic Ni(II) imprinted adsorbents had good reusability.

3.4 Adsorption mechanism

To further elaborate the adsorption mechanism, the chemical states of functional groups before and after Ni adsorption by Fe_3O_4@void@IIP-Ni(II) were investigated by FT-IR, XPS and and DFT calculation. The FT-IR results of the adsorbents before and after adsorption are shown in Fig. 4A, where Fig. 4A(f) shows Fe_3O_4@void@IIP-Ni(II) without Ni(II) adsorption, and Fig. 4A(e) shows Fe_3O_4@void@IIP-Ni(II) after Ni(II) adsorption. Compared

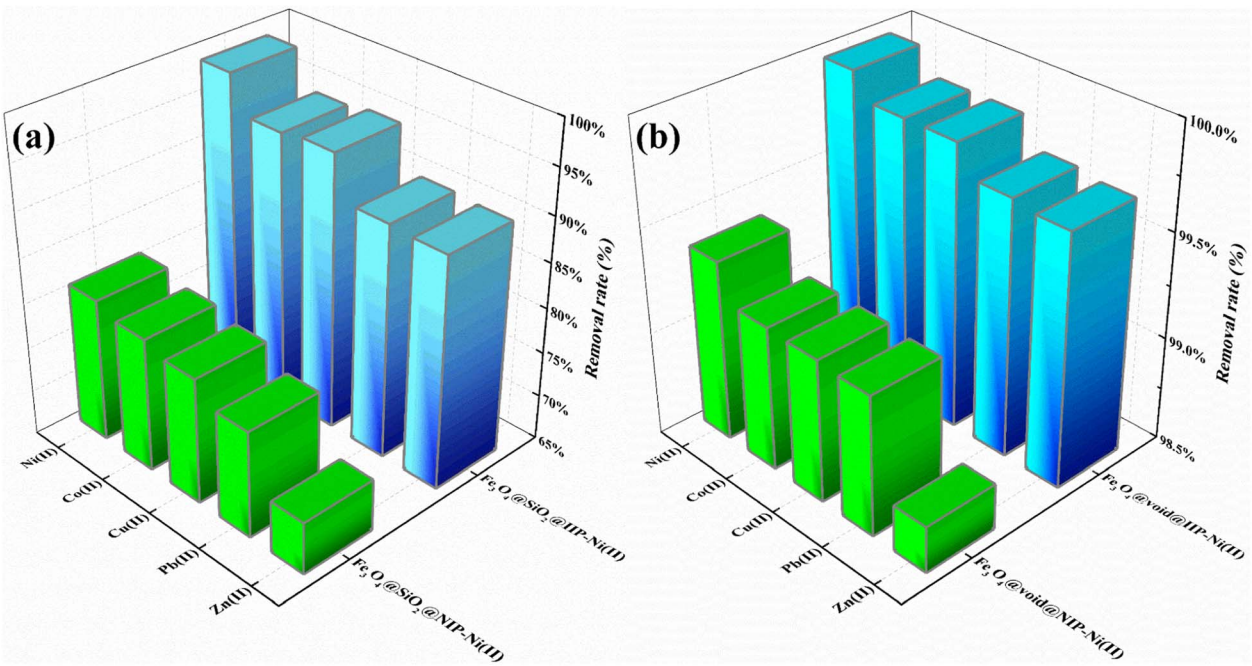

Fig. 6 Removal rate of ions in mixed solution by (a) Fe_3O_4@SiO_2@IIP-Ni(II) and Fe_3O_4@SiO_2@NIP-Ni(II); (b) Fe_3O_4@void@IIP-Ni(II) and Fe_3O_4@void@NIP-Ni(II).

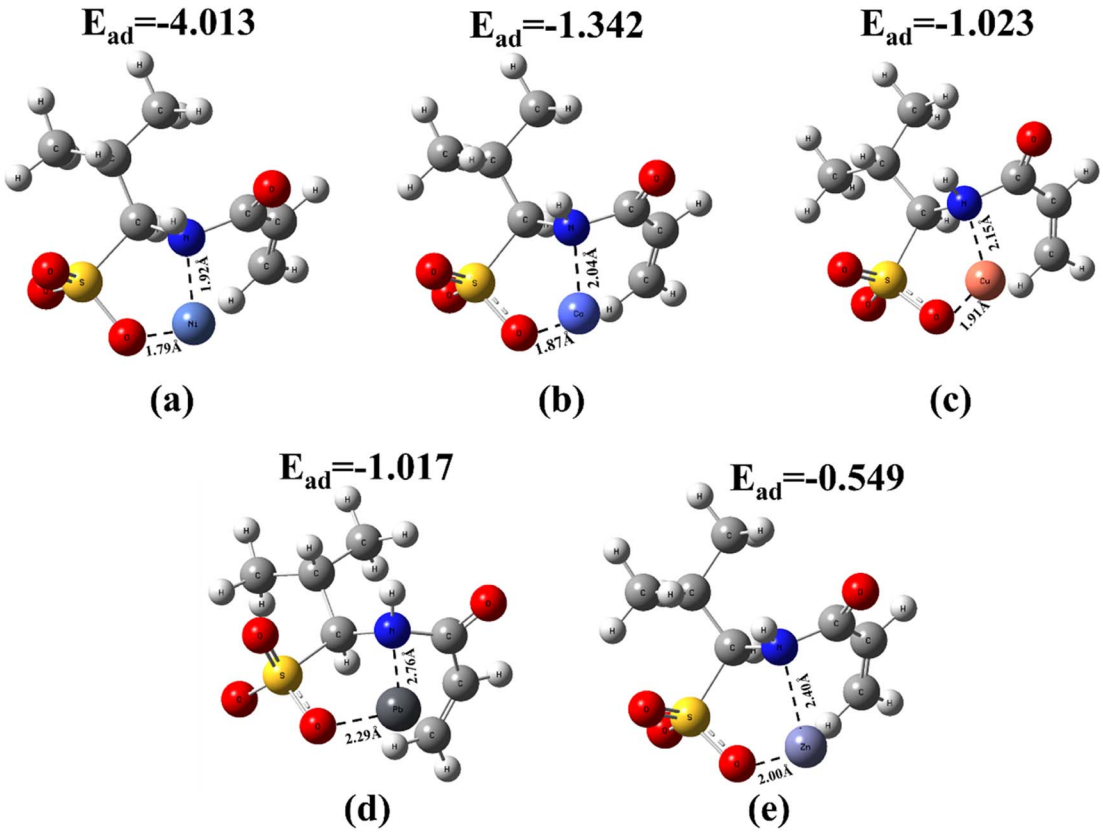

Fig. 7 Binding energies of different ions to AMPS (a) AMPS-Ni(II), (b) AMPS-Co(II), (c) AMPS-Cu(II), (d) AMPS-Pb(II), (e) AMPS-Zn(II).

with Fig. 4A(e), the absorbance of N-H at 3426 cm^{-1} was significantly enhanced, and the absorbance of N–H at 1537 cm^{-1} decreased and shifted. In addition, similar changes were observed for S=O at 1198 cm^{-1}, 1044 cm^{-1} and S–O bond at 624 cm^{-1}. It can be inferred that the adsorption of Ni(II) is mainly due to the coordination between –NH and $-SO_3H$ of AMPS and Ni(II) in the imprinted adsorbent.

The XPS results further clarified the changes of functional groups of Fe_3O_4@void@IIP-Ni(II) before and after adsorption of Ni(II) (Fig. 8). Fig. 8a shows the XPS survey spectrum before and after Ni(II) adsorption. The appearance of the Ni 2p peak after adsorption indicated that Ni(II) has been successfully absorbed. The high-resolution XPS spectrum of O 1s (Fig. 8b) has two peaks at 531.66 eV and 530.21 eV, which were $-SO_3H$ and –N–C=O in AMPS, respectively.[39] After the adsorption of Ni(II), the binding energy of these groups changed and shifted to 532.43 eV and 531.40 eV, respectively, which means that these groups participated in the adsorption of Ni(II). As for the N1s (Fig. 8c), a significant difference was observed before and after the adsorption of Ni(II). Before adsorption, N 1s had two peaks at 400.24 eV and 398.52 eV, which were ascribed to $-NH_2^+R$ and –NHR groups respectively. After adsorption, a new peak appeared at 399.94 eV, indicating the existence of chelation between Ni(II) and the nitrogen-containing groups, where the lone pair electrons of N formed coordination bonds with Ni(II).[40] The XPS spectrum of S 2p is shown in Fig. 8d. Two apparent peaks at 168.78 eV and 167.48 eV corresponded to $-SO_3H$ and $-SO_3^-$ groups of the sulfonic acid group in AMPS, respectively.[41] After adsorption, the binding energies of the two groups were increased to 169.49 eV and 168.34 eV, respectively, which indicated that Ni(II) coordinated with sulfonic acid group. As a result, it can be speculated that the adsorption of Ni(II) on Fe_3O_4@void@IIP-Ni(II) was the result of the co-coordination of O atoms of the sulfonic acid groups and N atoms of –N–C=O groups in AMPS with Ni(II).

The adsorption mechanism was further studied by DFT calculation. The optimized structures of the complexes formed by the functional groups with Ni(II) are shown in Fig. S6.† It can be seen from the binding energy that when Ni(II) coordinates with the N atom on the AMPS and the O atom on the sulfonic acid group (−4.013 eV), the complex structure is more stable than that with two O atoms on the sulfonic acid group (−3.863 eV). To further verify the chelating sites of the $AMPS^-$ molecule, the Fukui functions (f^-) of the coordination atoms was also calculated (Fig. 9a and Table S4†). The results showed that the N atom of –N–C=O group and the O atom of S–O group on AMPS molecule had higher f^- values (0.2744 and 0.1135, respectively), indicating that the N atom and the O atom of AMPS molecule are the preferred chelating sites for Ni(II), and they are more likely to lose electrons and be attacked by Ni(II). This calculation result is in well agreement with the XPS result.

The contour plots of highest occupied molecular orbital (HOMO) and lowest unoccupied orbital (LUMO) of $AMPS^-$ and AMPS-Ni(II) are shown in Fig. 9b. The HOMO of $AMPS^-$ before

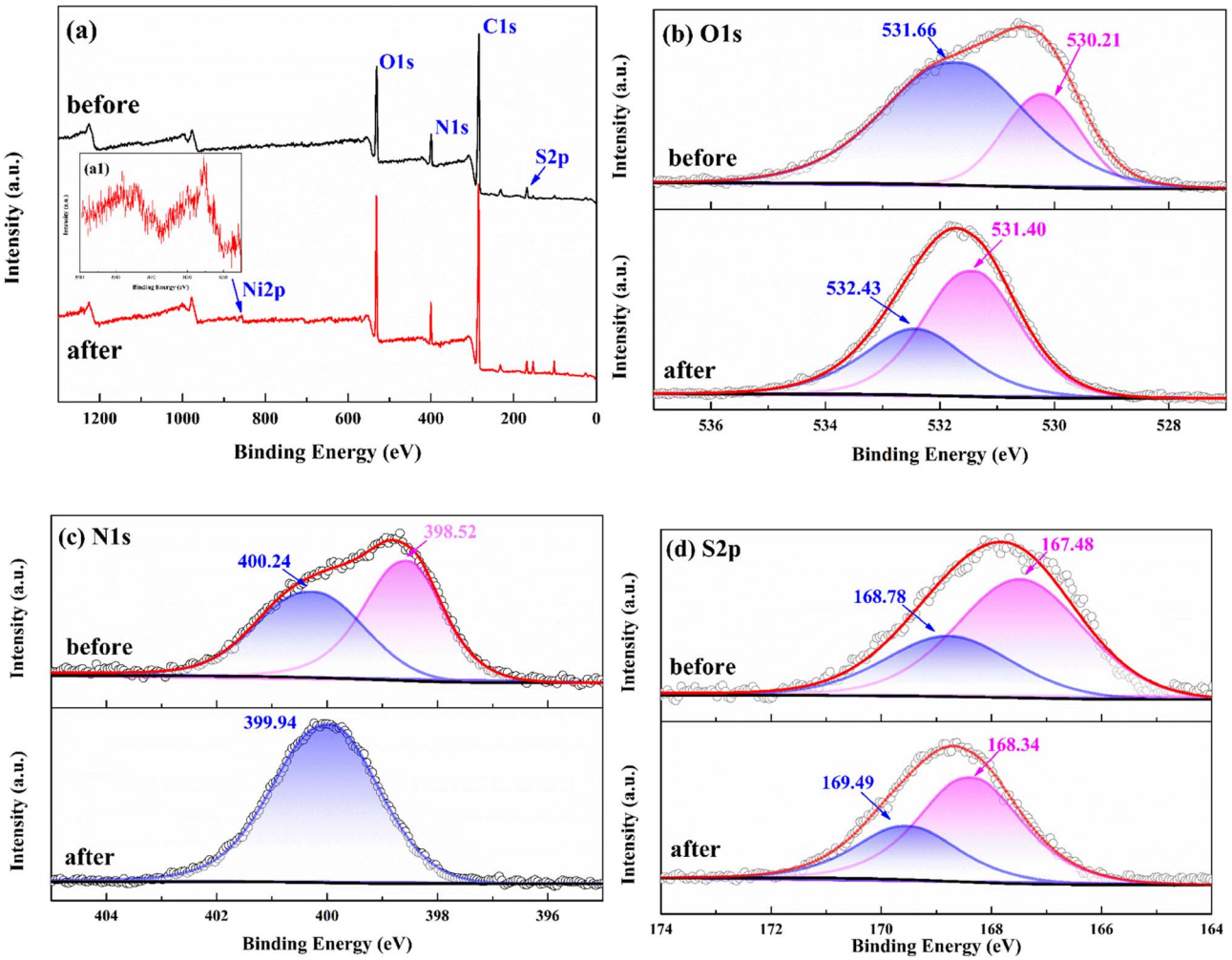

Fig. 8 XPS survey spectrum of IIP before and after Ni(II) adsorption (a), and high-resolution XPS of O 1s (b), N 1s (c), and S 2p (d) of IIP before and after adsorption of Ni(II).

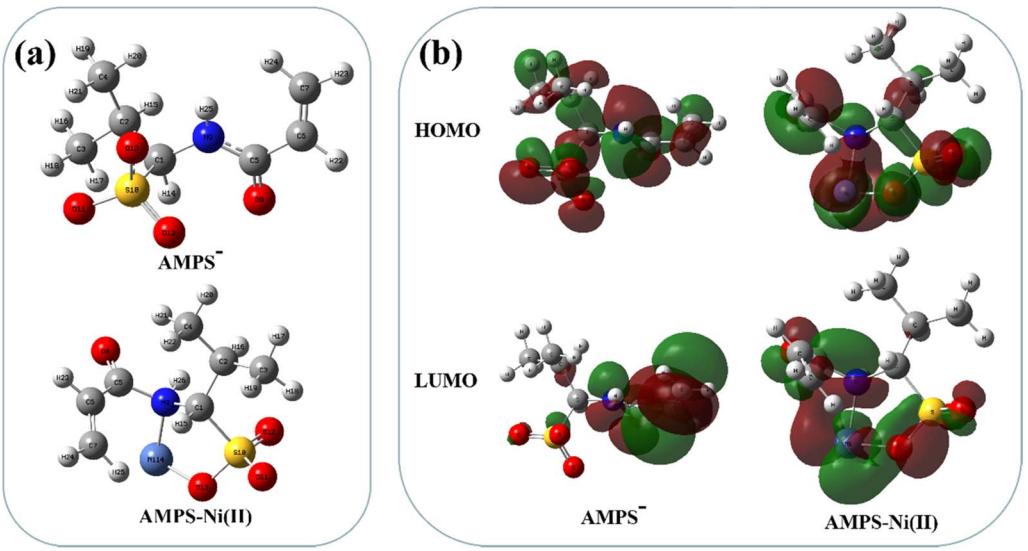

Fig. 9 Structural optimization of $AMPS^-$ and AMPS-Ni(II) (a), and contour plots of HOMO and LUMO of $AMPS^-$ and AMPS-Ni(II) (b).

adsorption was distributed on each atom, while after adsorption of Ni(II), the HOMO was concentrated near Ni(II), N and sulfonic acid groups, and their adjacent atoms. The LOMO of $AMPS^-$ was distributed in the positions of double bonds and N atoms of AMPS, after the adsorption of Ni(II), it was concentrated in the attachment of Ni atoms, double bonds and sulfonic acid groups. The changes of the HOMO and LUMO before and after adsorption confirms the charge transfer in the adsorption process.[42] The adsorption mechanism can also be reflected by the change of bond length and Wiberg bond order before and after adsorption, and the results are listed in Table S5.† It can be found that after the adsorption of Ni(II), the bond lengths of S–O bonds on the sulfonic acid groups and C–N bonds near the N atoms lengthened, and their Wiberg bond order weakened. This is due to the fact that the transfer of electrons from O and N atoms to the vacant orbitals of Ni(II) after the adsorption of Ni(II).[43]

3.5 Application in real water sample

The prepared magnetic rattle-type materials were applied to collect Ni(II) in real lake water sample from Tingxin lake of Kunmming University (Kunming, China). The nickel content in the lake water samples founded 0.47 μg L^{-1}. When 100 mg Fe_3O_4@void@IIP-Ni(II) or Fe_3O_4@void@NIP-Ni(II) was added to 10 mg L^{-1} 50 mL of water sample and shaken at 25 °C for 1 h, the initial concentration of Ni(II) detected by ICP-OES was 10.58 mg L^{-1}. After sorbents treatment, the amount of residual Ni(II) was almost zero, and the removal efficiency of Ni(II) in the actual water sample was close to 100%. The results validated the suitability of the magnetic rattle-type materials to remove Ni(II) from actual water.

4. Conclusion

In the present study, a novel magnetic rattle-type ion-imprinted polymer (Fe_3O_4@void@IIP-Ni(II)) was prepared for selective adsorption of Ni(II). The maximum adsorption capacity is 44.64 mg g^{-1} at the optimal pH of 6.0, and the adsorption reaches equilibrium in about 10 min. The removal rate of Ni(II) in a trace amount of mixed solution is as high as 99.97%, and Fe_3O_4@void@IIP loaded with Ni(II) can be easily separated from water solution in the presence of an applied magnetic field. The selectivity coefficients (k) for Ni(II)/Zn(II) is as high as 9.69, which is ascribed to the imprinting effect. Fe_3O_4@void@IIP-Ni(II) could be reused to adsorb Ni(II) from aqueous solutions, and the recovery of Ni(II) ions on Fe_3O_4@void@IIP-Ni(II) was maintained at about 95% after 6 adsorption–desorption cycles. The adsorption process of Ni(II) on Fe_3O_4@void@IIP-Ni(II) can be well described by Langmuir and Pseudo-secondary kinetic models, it was an endothermic, entropy-increasing and spontaneous process. The results of FT-IR, XPS and DFT calculations showed that O atoms of the sulfonic acid groups and N atoms of –N–C=O groups in AMPS played a dominant role in the adsorption of Ni(II), and the functional monomer AMPS has a high coordination ability for Ni(II). Furthermore, the imprinted polymer can also be used to adsorb trace Ni(II) in real water samples. To sum up, Fe_3O_4@void@IIP-Ni(II) proves to be a suitable adsorbent for the selective removal of trace Ni(II) from mixed solutions due to its magnetic properties and easy separation and recovery from the solution, which is benefit to energy saving, environmental protection and reuse. This work proposes a new method for guiding the adsorption mechanism and determining the adsorption configuration of imprinted adsorbents using DFT calculations.

Author contributions

The manuscript was written through contributions of all authors. All authors have given approval to the final version of the manuscript.

Conflicts of interest

There are no conflicts to declare.

Acknowledgements

This study was financially supported by the Applied Basic Research Project of Yunnan Province (No. 202001BA070001-192, 202001BA070001-120, ZX20220099), the Scientific Research Project of Kunming University (No. YJL20025), and the Scientific Research Fund of Education Department of Yunnan Province (No. 2019J0566, 2022Y747).

Notes and references

1 P. Shao, D. Liang, L. Yang, H. Shi, Z. Xiong, L. Ding, X. Yin, K. Zhang and X. Luo, *J. Hazard. Mater.*, 2020, **387**, 121676.
2 B. Gupta, A. Mishra, R. Singh and I. S. Thakur, *Environ. Technol. Innovation*, 2021, **21**, 101278.
3 W. Liu, M. Zhang, X. Liu, H. Zhang, J. Jiao, H. Zhu, Z. Zhou and Z. Ren, *Ind. Eng. Chem. Res.*, 2020, **59**, 6033–6042.
4 H. X. He, Q. Gan and C. G. Feng, *Chin. J. Polym. Sci.*, 2018, **36**, 462–471.
5 X. Shen and X. Chen, *Sep. Purif. Technol.*, 2019, **223**, 88–95.
6 M. A. Islam, M. R. Awual and M. J. Angove, *J. Environ. Chem. Eng.*, 2019, **7**, 103305.
7 Z. Yao, P. Shao, D. Fang, J. Shao, D. Li, L. Liu, Y. Huang, Z. Yu, L. Yang, K. Yu and X. Luo, *Chem. Eng. J.*, 2022, **427**, 131470.
8 T. Kim, T. K. Kim and K. D. Zoh, *J. Water Process Eng.*, 2020, **33**, 101109.
9 J. Lu, Y. Qin, Y. Wu, M. Meng, Y. Yan and C. Li, *Environ. Sci.: Water Res. Technol.*, 2019, **5**, 1626–1653.
10 A. Ma, A. Abushaikha, S. J. Allen and G. Mckay, *Chem. Eng. J.*, 2019, **358**, 1–10.
11 W. Liu, Z. An, L. Qin, M. Wang, X. Liu and Y. Yang, *Chem. Eng. J.*, 2021, **411**, 128477.
12 M. Li, C. Feng, M. Li, Q. Zeng and Q. Gan, *Hydrometallurgy*, 2015, **154**, 63–71.
13 P. He, H. Zhu, Y. Ma, N. Li, X. Niu, M. Wei and J. Pan, *Chem. Eng. J.*, 2019, **367**, 55–63.

14 P. Yang, H. Cao, D. Mai, T. Ye, X. Wu, M. Yuan, J. Yu and F. Xu, *React. Funct. Polym.*, 2020, **151**, 104569.
15 L. Hou, C. Yang, X. Rao, L. Hu and X. Zhu, *Colloids Surf., A*, 2021, **625**, 126949.
16 E. Kazemi, S. Dadfarnia, A. Shabani and M. Ranjbar, *Food Chem.*, 2017, **237**, 921–928.
17 Z. Cheng, H. Lyu, B. Shen, J. Tian, Y. Sun and C. Wu, *Chemosphere*, 2022, **288**, 132581.
18 X. Li, X. Ma, R. Huang, X. Xie, L. Guo and M. Zhang, *J. Sep. Sci.*, 2018, **41**, 2837–2845.
19 S. Buyuktiryaki, R. Kecili and C. Hussain, *TrAC, Trends Anal. Chem.*, 2020, **127**, 115893.
20 X. Wang, J. Feng, Y. Bai, Q. Zhang and Y. Yin, *Chem. Rev.*, 2016, **116**, 10983–11060.
21 W. Zhao, H. Chen, Y. Li, L. Li, M. Lang and J. Shi, *Adv. Funct. Mater.*, 2008, **18**, 2780–2788.
22 R. Yang, Y. Liu, X. Yan, S. Liu and H. Zheng, *J. Mater. Chem. A*, 2016, **4**, 9807–9815.
23 R. Yang, Y. Liu, X. Yan and S. Liu, *Talanta*, 2016, **161**, 114–121.
24 J. P. Fan, J. X. Yu, X. M. Yang, X. H. Zhang, T. T. Yuan and H. L. Peng, *Chem. Eng. J.*, 2018, **337**, 722–732.
25 J. Lu, Y. Y. Qin, Y. L. Wu, M. N. Chen and Y. Yan, *Chem. Eng. J.*, 2021, **417**, 128085.
26 W. Lai, K. Zhang, P. Shao, L. Yang, L. Ding, S. G. Pavlostathis, H. Shi, L. Zou, D. Liang and X. Luo, *J. Hazard. Mater.*, 2019, **379**, 120791.
27 C. Ni, Q. Liu, Z. Ren, H. Hu, B. Sun, C. Liu, P. Shao, L. Yang, S. G. Pavlostathis and X. Luo, *J. Environ. Chem. Eng.*, 2021, **9**, 106701.
28 H. He, Q. Gan and C. Feng, *RSC Adv.*, 2017, **7**, 15102–15111.
29 Z. Chang, L. Yang, K. Zhang, W. Hu, C. Ni, P. Shao, H. Shi, K. Yu and X. Luo, *Chem. Eng. J.*, 2021, **416**, 129144.
30 Y. Cheng, J. Nie, J. Li, H. Liu, Z. Yan and L. Kuang, *Food Chem.*, 2019, **287**, 100–106.
31 M. Hussain, T. Rehan, K. W. Goh, S. I. Shah, A. Khan, L. C. Ming and N. Shah, *Polymers*, 2022, **14**, 2681.
32 Y. H. Gad, *Radiat. Phys. Chem.*, 2008, **77**, 1101–1107.
33 N. Sun, R. Lei, J. Xu, S. C. Kundu, Y. Cai, J. Yao and Q. Ni, *J. Mater. Sci.*, 2019, **54**, 3319–3330.
34 F. Goudarzi and P. Hejazi, *React. Funct. Polym.*, 2019, **143**, 104322.
35 Y. Cui, W. Kang, L. Qin, J. Ma, X. Liu and Y. Yang, *Chem. Eng. J.*, 2020, **397**, 125480.
36 H. Hu, Z. Ren, Y. Xi, L. Fang, D. Fang, L. Fang, P. Shao, H. Shi, K. Yu and X. Luo, *Chem. Eng. J.*, 2021, **420**, 129611.
37 R. D. Harter, *Soil Sci. Soc. Am. J.*, 1983, **47**, 47–51.
38 Y. Chen, X. Ma and J. Peng, *Carbohydr. Polym.*, 2021, **271**, 118435.
39 T. Lu, Y. Zhu, Y. Qi, W. Wang and A. Wang, *Int. J. Biol. Macromol.*, 2018, **106**, 870–877.
40 J. Wang and F. Liu, *Chem. Eng. J.*, 2014, **242**, 117–126.
41 J. Ma, Y. Zhang, Y. Tang, Y. Wei, Y. Liu and C. Liu, *Water Sci. Technol.*, 2018, **78**, 982–990.
42 B. Zhang, Y. Niu, L. Li, W. Xu, H. Chen, B. Yuan and H. Yang, *Microchem. J.*, 2019, **151**, 104220.
43 M. Li, C. Zhao, Q. Feng, J. Feng and X. Meng, *Chem. J. Chin. Univ.*, 2021, **42**, 3680–3691.